MESOSPHERE DYNAMICS WITH GRAVITY WAVE FORCING: 1, DIURNAL AND SEMI-DIURNAL TIDES

by

H. G. Mayr[1], J. G. Mengel[2], K. L. Chan[3], and H. S. Porter[4]

[1]NASA Goddard Space Flight Center, Greenbelt, MD

[2]SM&A Corporation, Vienna, VA

[3]Hong Kong University of Science and Technology, Hong Kong, China.

[4]Furman University, Greenville, SC

Prepared for Publication

in

Journal of Atmospheric and Solar Terrestrial Physics

September 2000

ABSTRACT: We present results from a nonlinear, 3D, time dependent numerical spectral model (NSM), which extends from the ground up into the thermosphere and incorporates Hines' Doppler Spread Parameterization for small-scale gravity waves (GW). Our focal point is the mesosphere that is dominated by wave interactions. We discuss diurnal and semi-diurnal tides in the present paper (Part I) and planetary waves in the companion paper (Part II). To provide an understanding of the seasonal variations of tides, in particular with regard to gravity wave processes, numerical experiments are performed that lead to the following conclusions: 1.) The large semiannual variations in the diurnal tide (DT), with peak amplitudes observed around equinox, are produced primarily by GW interactions that involve, in part, planetary waves. 2.) The DT, like planetary waves, tends to be amplified by GW momentum deposition, which reduces also the vertical wavelength. 3.) Variations in eddy viscosity associated with GW interactions tend to peak in late spring and early fall and can also influence the DT. 4.) The semidiurnal tide (SDT), and its phase in particular, is strongly influenced by the mean zonal circulation. 5.) The SDT, individually, is amplified by GW's. But the DT filters out GW's such that the wave interaction effectively reduces the amplitude of the SDT, effectively producing a strong nonlinear interaction between the DT and SDT. 6.) Planetary waves generated internally by baroclinic instability and GW interaction produce large amplitude modulations of the DT and SDT.

I. Introduction

The fundamental properties of tides are well understood (Chapman and Lindzen, 1971; Volland, 1986), and theoretical models have been used extensively to study the effects caused by the mean zonal circulation and temperature variations, by eddy viscosity and gravity wave interactions (e.g., Lindzen and Hong, 1974; Forbes, 1995; Forbes *et al.*, 1991; Forbes and Hagan, 1988; Forbes and Vial, 1989; Hagan, 1996; Hagan *et al.*, 1995; Vial and Forbes, 1989; Akmaev *et al.*, 1996; Fritts, 1995a, b; Miyahara and Forbes, 1991; Geller et al., 1997; Mayr et al., 1998, 1999; Akmaev, 2000).

Measurements from the ground (e.g., Avery *et al.*, 1989; Mason *et al.*, 1989; Vincent *et al.*, 1989) and with the UARS spacecraft (Hays *et al.*, 1994; McLandress *et al.*, 1996; Burrage *et al.*,

1995a, b) have shown that the diurnal tides in the Mesosphere Lower Thermosphere (MLT) exhibit large seasonal variations that are modulated by planetary waves (e.g., Forbes, 1995, Fritts, 1995b). The variations in the diurnal tide in particular exhibit large amplitude maxima during equinox, and these have been attributed specifically to postulated variations in eddy viscosity (e.g., Geller et al., 1997; Yudin et al., 1997), to gravity wave momentum deposition (Mayr et al., 1998, 1999) and to variations in eddy viscosity associated with gravity wave interaction (Akmaev, 2000). The physical processes responsible for modulating this tide, however, are not yet fully understood. And much less understood are the variations observed in the semidiurnal tide. This has been the impetus for the present paper, in which we shall present numerical experiments designed to provide insight in particular with regard to gravity wave processes that are playing an important role in the dynamics of the upper mesosphere.

In Section II, we shall discuss the overall organization and dynamical components of the model, the properties of the numerical model, the adopted gravity wave parameterization, and the approach taken in our analyses. In Section III, we then present computed wind fields that characterize the diurnal tide and delineate with numerical experiments the contributions of different processes including those associated with the excitation of planetary waves. In Section IV, we present numerical results to analyze the semidiurnal tide, including the contribution made by the diurnal tide. In Section V, we summarize the results and enumerate the conclusions. In a companion paper, we shall discuss numerical results for the planetary waves that are generated by dynamical processes in the mesosphere.

II. Model and Analysis Approach

We illustrate the organization of our model in Figure 1. The Numerical Spectral Model (NSM), introduced by Chan et al. (1994a, b), is three dimensional, time-dependent and nonlinear, and it is formulated with vector spherical harmonics. Incorporated into this model is the Doppler Spread Parameterization for small-scale gravity waves (GW), developed by Hines (1994a, b), which provides the wave momentum source and related eddy diffusivity. The model computes the interacting dynamical components for the zonal mean ($m = 0$), and the tides and planetary waves ($m = 1 - 4$).

The NSM extends from the ground up into the thermosphere and computes the wind field and the perturbations of globally averaged temperature and density variations. Homogeneous boundary conditions are applied, i.e., vanishing vertical and horizontal winds at the Earth's surface, and vanishing vertical gradients of temperature and horizontal winds at the upper boundary where molecular heat conduction and viscosity dominate. For the zonal mean (m = 0), the solar UV heating above 15 km is taken from Strobel (1978); tropospheric heating is not accounted for. The diurnal tides (m = 1 and 2) are thermally excited by solar radiation absorbed in the water vapor layer near the ground and by ozone around 50 km [taken from Forbes and Garrett (1978)], and by UV and EUV radiation in the thermosphere. Energy loss by IR radiation is parameterized with Newtonian cooling taken from Zhun (1988). Ion drag and molecular dissipation are accounted for in the thermosphere. Normally the upper boundary of the NSM is at 400 km, but in the present application it is at 250 km so that the model can be run more efficiently to carry out the various numerical experiments. To account for the short vertical wavelength of the propagating tides, the vertical step size and related time step are chosen to be about 0.45 km and less than 10 minutes respectively. Spherical harmonics are carried in the model up to order $l = 12$, which corresponds to a grid point resolution of about 7.5° in the meridional direction.

The DSP is applied in the model under the simple assumption that the GW flux emanating at the surface is isotropic and independent of latitude and season. The parameters describing the GW momentum deposition are typically taken from the middle of the proposed ranges, i.e., $\Phi_1 = 1.5$ and $\Phi_2 = 0.3$ (see Hines, 1997a, b). In the DSP, the GW momentum flux is proportional to the horizontal wavenumber k*; its value is taken to be $(60\ \text{km})^{-1}$, which is in the middle of the recommended range of the DSP [$(100\ \text{km})^{-1} < k* < (10\ \text{km})^{-1}$, see Hines (1997a, b)]. The GW momentum flux is also proportional to σ_h^3 at the initial height, where σ_h is the rms total horizontal wind variability. This value is chosen to produce about 2.0 m/s at 20 km (compared to the earlier 2.5 m/s), in rough agreement with the values reported by Allen and Vincent (1995) at mid latitudes. Compared to the earlier model, the adopted GW momentum flux initiated at the Earth's surface thus has been reduced by about a factor of 2. In the DSP, the GW momentum source as well as the related diffusivity and energy source (not considered presently) are derived by integrating over the incident wave spectrum, which is described at the initial height in terms

of the minimum vertical wavenumber m_m and the cut-off wavenumber m. We choose m_m = (3 km)$^{-1}$ [(2 km)$^{-1}$ suggested in the DSP] to produce the height dependent eddy diffusivity, K, that levels off at altitudes above 100 km as shown in Figure 2. Consistent with K, the GW momentum source also levels off at higher altitudes, but it levels off in a way that causes numerical problems. To get around this problem, we adopt the scaling procedure discussed by Mayr *et al.* (1998) [important mainly at altitudes above 90 km], which preserves approximately the relationship between GW momentum source and eddy diffusivity.

An integral part of the model presented here is that it describes the various dynamical components of the atmosphere as they interact with each other. Of particular importance for our understanding of the diurnal tides and planetary waves are the mean zonal circulation and temperature variations, which are affected significantly by gravity wave processes. As demonstrated by Lindzen (1981), GW momentum deposition in the background flow can account to a large extent for the observed anomalous temperature minimum in the summer hemisphere and the associated reversal in the zonal circulation. A basic tenet of our modeling approach is therefore that the chosen GW parameters essentially reproduce these features. This is demonstrated with Figure 3, which reproduces for December solstice the computed temperature variations and zonal winds in the altitude range between 20 and 110 km. Near 90 km, the temperature decreases at high latitudes from 200 K in winter to 140 K in summer. The zonal winds tend to reverse at altitudes above, turning eastward in summer and westward in winter. These results are in substantial agreement with observations.

As illustrated in Figure 1, GW's affect the diurnal tides in numerous ways and this complicates our understanding. As pointed out in our discussion of Figure 3, GW's are of central importance for the mean zonal circulation (m = 0), and that circulation in turn is important for the seasonal variations of the tides. In addition, as illustrated in Figure 1, the GW's also affect the tides through channels that do not involve the mean zonal circulation.

To provide an understanding of GW processes, we adopt a modeling strategy that allows us isolate their effects on the tides and planetary waves from those affecting the mean zonal cicrulation. For this purpose, we adopt a two-prong approach: 1) The dynamical components in the model (Figure 1) are computed self consistently, i.e., their interactions are fully accounting for under the influence of GW's. 2) The zonal mean (m = 0) component for temperatuire variations and wind fields, varying with season, are then fed in weekly intervals into the model

to compute for m > 0 the tides and planetary waves under different assumptions concerning the GW interactions. Linear interpolation in this step-wise procedure assures that the m = 0 component for temperature and wind fields are continuous. But the first and higher order time derivatives are discontinuous, and this introduces apparently some numerical noise so that the computed tides and planetary waves differ from those computed self consistently. For the tides the differences are small. For the planetary waves, generated largely by baroclinic instability, the amplitudes produced with the 'step-procedure' are systematically larger than those computed self consistently . Nevertheless, the reproduces reasonably well reproduces the characteristic seasonal and height variations of the planetary waves and it allows us to properly assess the importance of GW processes.

III. Diurnal Tide

General Properties: With constant eddy viscosity shown in Figure 2, taken to be independent of latitude and season, we ran the model for 3 years. At 95-km altitude, the computed amplitude for the meridional winds of the diurnal tide (averaged over 15 days) are shown in Figure 4. It reveals peaks near 20° latitude, which is characteristic of the propagating tide, S_1^1, that is expected to dominates at this altitude according to classical tidal theory (e.g., Chapman and Lindzen, 1971). We emphasize that in our model no restrictive assumption is made about tidal modes; linear as well as nonlinear mode coupling are accounted for implicitly. As we had reported earlier (Mayr et al., 1998), the model also produces wind amplitudes that peak near equinox, which is in substantial agreement with the analysis of measurements on the UARS spacecraft (Hays et al., 1994; Burrage et al. 1997) carried out with the HRDI instrument (Hays et al., 1993). The model results are shown in Figure 5 with more detail at 18° latitude (a Gaussian point), where we present also the computed phase of the meridional winds and the amplitude modulation due to planetary waves. The phase agrees, on average, with the UARS measurements and shows a distinctive seasonal variation, occurring later during the winter and summer months than during equinox when the amplitude peaks.

To provide a more detailed picture, we present with Figure 6 the altitude variations of computed amplitudes plotted with logarithmic contour intervals. This reveals a complicated

pattern of seasonal variations, exhibiting in different altitude regimes minima both during summer and winter months. 1.) At altitudes around 40 km, a minimum develops in winter when there is less thermal excitation by absorbed solar radiation. However, it is by no means clear that this is the principal cause. To determine that one would need to investigate what the amplitude patterns are without GW forcing and seasonal variations in the tidal excitation. 2) At altitudes between 60 and 70 km a minimum develops in summer, which could be produced by absorption of this westward propagating tide as it encounters westward zonal winds in the region (see Figure 3). These minima during solstice conditions at lower altitudes do contribute to the formation of the equinoctial amplitude maxima at altitudes around 95 km observed on UARS and reproduced in our model.

Analyses: To shed light on the processes that produce the characteristic seasonal variations in the diurnal tide, we carried out numerical experiments in the way discussed earlier. For this purpose, we feed the seasonal variations of the zonal mean (m = 0) temperature and wind fields (computed self consistently with GW forcing) into the 3D model and compute the diurnal tide with and without GW forcing. The results are presented in Figure 7 for amplitude and phase, based on 5-day averages of the computed meridional winds. Without GW forcing, pronounced minima develop in winter that are even deeper than those produced with the wave interaction. But during summer, the amplitudes are much larger and during equinox they are smaller. The seasonal variations without GW interaction do not resemble the observations (Burrage et al., 1995), and this demonstrates the important role GW play for our model results. The computed phase without GW forcing occurs about 4 hour later.

In contrast to the Rayleigh friction parameterization, the GW source from the DSP causes acceleration by depositing momentum in proportion to the vertical gradients of the winds they encounter. This acceleration occurs preferentially where the winds in the direction of wave propagation increase. Waves propagating to the north add momentum in regions where the winds are northward and increase with height, and southward propagating waves accelerate the southward flow. The combined actions of northward and southward propagating waves thus act to increase the wind amplitudes especially at higher altitudes (and the same holds for the eastward and westward propagating waves). Acceleration in the region where the winds increase with height thus reduces the vertical wavelength of the tide and this shifts the phase to earlier local times as seen in Figure 7.

In the upper mesosphere, planetary waves (PW) with amplitudes comparable to those of the diurnal tides are observed and generated in the model. An example of that is shown at in Figure 8, where we present the meridional winds for wavenumber m = 3 computed with and without GW momentum source. Consistent with observations, this wave (like the one for m = 4) appears preferentially during solstice condition, and this has been attributed to the baroclinic instability (Plumb, 1983) as confirmed by the modeling studies of Norton and Thuburn (1997, 1999). That being true, one should expect then that such PW's could be excited at the expense of the diurnal tide and thus contribute to produce the observed seasonal variations. To examine this process, we have artificially suppressing the m = 3, 4 planetary waves, and the results of the numerical experiment are presented in Figure 9. This shows indeed that the tidal amplitude is larger in summer when the PW's are not excited. The excitation of these PW's does contribute significantly to the seasonal variations of the tide as Norton and Thuburn (1996, 1999) had concluded.

In more than one way, however, GW processes are the actual cause for the above-described interaction involving PW's. Momentum deposited by GW causes the latitudinal temperature reversal in the upper mesosphere, which produces the baroclinic instability (Plumb, 1983) that is feeding the PW's. As shown in Figure 8, however, GW are also involved directly in generating PW's. With the GW source, the PW amplitudes are much larger and this is understandable considering that GW's tend to amplify the vertical wind shears they encounter. In summer and to a lesser extent in winter, the PW's initiated by the baroclinic instability are amplified by GW's. The GW's thus absorbed by PW's are not available to amplify the diurnal tide and its amplitude is therefore reduced in summer as shown in Figure 9.

Presently, our model cannot account for the latitudinal variations in the eddy viscosity, K. We have computed the variations provided by the DSP at 18° latitude and present in Figure 10 the ratio relative to the K adopted in the model (Figure 2). This shows that below 90 km the eddy viscosity is larger during summer and winter months, which would tend to reduce the amplitude of the diurnal tide during solstice relative to equinox. At higher altitudes, however, K is larger during equinox, and this would move the seasonal variations of the tide in the opposite direction. We have carried out a computation in which the K variations, as shown in Figure 10, were assumed to apply to the entire globe, which probably overestimates the effect. The resulting seasonal variation in the diurnal tide, not shown here, were not significantly different

from the standard solution presented here. At 95 km, the amplitudes are somewhat larger during spring and summer months but are virtually the same in fall and winter.

IV. Semi-diurnal Tide

General Properties: The semidiurnal tide has been observed with radar measurements from the ground at northern mid latitudes (Jacobi et al., 1999) and with satellite measurements on UARS (Burrage et al., 1995b; McLandress et al., 1997) . Zonal wind data at altitudes between about 80 and 105 km reveal seasonal variations with amplitudes between 15 and 30 m/s that peak in winter and in fall. In this altitude range the phase (eastward) is also observed to vary considerably but is typically around 10:00 LT in winter and 7:00 LT in summer.

Modeling the semi-diurnal tide poses difficulties that go considerably beyond those encountered with the diurnal tide, and with our model we are far from having a reasonably good grasp on this problem. The semidiurnal tide in the upper mesosphere is significantly affected by the mean zonal circulation and its large seasonal variations. Initial results from a model with larger GW flux produced too large a reversal in the mean zonal circulation above 80 km, and the resulting phase of the semi-diurnal tide was nowhere close to that observed. As seen later, the semi-diurnal tide is also influenced significantly by the diurnal tide. Notwithstanding this strong interconnection between different dynamical components, which requires that observed phenomena are studied jointly and simulated with great care, we present here the computed zonal winds for the semidiurnal tide obtained under different conditions to provide some understanding of the physical processes involved.

In Figure 11 the zonal wind amplitudes are presented at 95 km and show large seasonal variations with peak values at mid latitudes that occur in winter. At lower latitudes, the amplitudes are generally smaller and tend to peak during the spring and fall seasons, revealing a pattern similar to that observed in the diurnal tide. To provide more details, we show in Figure 12 the computed zonal wind amplitude and phase for 48° latitude at 90 and 95 km altitude. The large amplitude modulations are due to planetary waves. At 95 km, the largest amplitudes clearly occur in winter. But at 90 km a pronounced secondary maximum also develops during the fall season, and this tendency is qualitatively consistent with the observations (Jacobi et al.,

1999). The computed phase variations of eastward winds are within the wide range of observed values.

In Figure 13, we show the height variations of computed amplitudes with logarithmic contour intervals. As is the case for the diurnal tide, this reveals at different altitudes complicated patterns in the seasonal variations that are difficult to understand. Between 50 and 75 km, the amplitudes are larger in summer than in winter, which is probably due to the seasonal variations in the thermal excitation produced by absorption of solar radiation in ozone. An increase also occurs in winter, though it is much weaker, and this may be caused as well by differential solar heating but with phase opposite to that in summer. At altitudes between 80 and 100 km the computed amplitudes are largest in winter.

Analyses: To provide some understanding, we present in Figure 14 solutions obtained with and without the seasonal variations of solar differential heating. The differences are small for most of the year, but during winter months the results reflect a significant increase in thermal excitation. This increase is understandable considering that during winter at higher latitudes the portion of the day decreases that is illuminated by solar radiation, which tends to increase the relative importance of the semi-diurnal heat source.

In contrast to the numerical experiment for the diurnal tide, turning off the GW momentum source does not affect much the semi-diurnal tide as shown in Figure 15. Except for a small increase of the tide in winter, there is no clear-cut trend in the seasonal variations. That GW's are less effective is understandable in principle, considering that the waves must compete with the inertial acceleration that is twice as large for the semi-diurnal tide than the diurnal tide. As shown in the following, however, GW actually do play an important role but in a different way.

With Figure 16, we present a numerical experiment in which the diurnal tide is not thermally excited. The result is that the amplitude of the semi-diurnal tide increases significantly throughout the year and in particular during the spring season. We interpret this to be the consequence of GW filtering, which comes into play primarily during the spring and fall seasons when the amplitude of the diurnal tide is largest. This interpretation is supported by an earlier experiment we had carried out (see Figure 3 of Mayr et al., 1999) in which the amplitude of the semi-diurnal tide was computed without the mean zonal circulation but with and without the diurnal tide, and without GW forcing. In principle, the diurnal tide could affect the semi-diurnal tide also through the non-linear fluid dynamics that is accounted for in the model. But this is not

the case. A control experiment without GW forcing shows that the semi-diurnal tide is not affected significantly by the presence or absence of the diurnal tide. Our analysis shows that GW's are involved to produce a strong non-linear interaction between the diurnal and semi-diurnal tides.

IV. Summary and Conclusions

The diurnal and semi-diurnal tides observed in the upper mesosphere reveal large seasonal variations that are not well understood. In the diurnal tide in particular, large amplitude variations are seen with peak amplitudes around equinox that have been attributed to postulated variations in eddy viscosity (Hagan et al., 1988; Yudin and Geller, 1993), gravity wave momentum deposition associated with wave filtering by the mean zonal circulation (Mayr et al., 1997, 1999) and variations in eddy viscosity associated with gravity wave breaking (Akmaev, 2000).

The paper presented is a follow-up on our earlier studies (Mayr et al., 1997, 1999) in that we make here an attempt to provide a better understanding of the gravity wave processes affecting the diurnal and semi-diurnal tides in the upper mesosphere. Our Numerical Spectral Model (NSM) incorporates the gravity wave (GW) momentum source from Hines' Doppler Spread Parameterization (DPS) and accounts for the associated height variations in the eddy viscosity. The latitudinal and seasonal variations of the eddy viscosity are not incorporated. We applied this model under different dynamical conditions and carried out numerical experiments that lead to the following conclusions.

Diurnal Tide:

1. Unlike the Rayleigh friction parameterization, the GW momentum source from the DSP causes acceleration by depositing momentum in proportion to the vertical gradients of the winds they encounter, and this amplifies the tides and reduces their vertical wavelength, causing the phase to be shifted to earlier local times.
2. The large semiannual variations in the diurnal tide, with maxima observed around equinox at 95 km altitude, are produced primary by the GW momentum source.

3. Planetary waves with zonal wave numbers m = 3, 4 (excited by the baroclinic instability) are greatly amplified by GW, and this contributes also to the seasonal variations of the diurnal tide.
4. Variations in eddy viscosity associated with the GW interaction tend to peak above 80 km in late spring and early fall, and this may also have an influence.

Semi-diurnal Tide:

1. The phase of this tide in particular is strongly influenced by the mean zonal circulation that in turn is significantly affected by the GW interaction in the mesosphere.
2. The seasonal variations in the excitation source are important for the seasonal variations of the tide at mid latitudes.
3. The semi-diurnal tide individually, without the presence of the diurnal tide, is amplified by the GW interaction in particular during the spring season.
4. With the diurnal tide present, the semi-diurnal tide is not affected significantly when the GW source is turned off.
5. From (3) and (4) the conclusion is drawn that GW filtering by the diurnal tide influences the semi-diurnal tide and thus produces effectively a strong non-linear interaction between the two tidal components.

Planetary waves, generated internally by the baroclinic instability and by GW interactions, produce amplitude modulations in the diurnal and semi-diurnal tides.

References

Akmaev, R. A., Simulation of large-scale dynamics in the mesosphere and lower thermosphere with the Doppler-spread parameterization of gravity waves: 2. Eddy mixing and the diurnal tide, *J. Geophys. Res.*, in press, 2000

Akmaev, R. A., J. M. Forbes, and M. E. Hagan, Simulation of tides with a spectral mesosphere/lower thermosphere model, *Geophys. Res. Lett.*, **23**, 2173, 1996

Avery, S. K., R. A. Vincent, A. Phillips, A. H. Manson, and G. R. Fraser, High latitude tidal behavior in the mesosphere and lower thermosphere, *J. Atm. Terr. Phys.*, **51**, 595, 1989

Burrage M. D., M. E. Hagan, W. R. Skinner, D. L. Wu, and P. B. Hays, Long-term variability in the solar diurnal tide observed by HRDI and simulated by the GSWM, *Geophys. Res. Lett.*, **22**, 2641, 1995a

Burrage M. D., D. L. Wu, W. R. Skinner, D. A. Ortland, and P. B. Hays, Latitude and seasonal dependence of the semidiurnal tide observed by the high-resolution Doppler imager, *J. Geophys. Res.*, **100**, 11313, 1995b

Chan, K. L., H. G. Mayr, J. G. Mengel, and I. Harris, A spectral approach for studying middle and upper atmospheric phenomena, *J. Atmos. Terr. Phys.*, **56**, 1399, 1994

Chapman, S., and R. S. Lindzen, *Atmospheric Tides*, D. Reidel, Hingham, MA, 1970

Forbes, J. M., and H. B. Garrett, Thermal excitation of atmospheric tides due to insolation absorption by O_3 and H_2O, *Geophys. Res. Lett.*, **5**, 1013, 1978

Forbes, J. M, and M. E. Hagan, Diurnal propagating tides in the presence of mean winds and dissipation: a numerical investigation, *Planet. Space Sci.*, **36**, 579, 1988

Forbes, J. M., and F. Vial, Monthly simulations of solar semidiurnal tide in the mesosphere and lower thermosphere, *J. Atm. Terr. Phys.*, **51**, 649, 1989

Forbes, J. M, J. Gu, and S. Miyahara, On the interactions between gravity waves and the diurnal propagating tide, *Planet. Space Sci.*, **39**, 1249, 1991

Forbes, J. M., Tidal and planetary waves, *Geophysical Monograph* **87**, 67, 1995

Fritts, D. C., Gravity wave-tidal interactions in the middle atmosphere: observations and theory, *Geophysical Monograph* **87,** 89, 1995a

Fritts, D. C., Gravity wave forcing and effects in the mesosphere and lower thermosphere, *Geophysical Monograph* **87,** 121, 1995b

Geller, M. A., V. A. Yudin, B. V. Khattatov, and M. E. Hagan, Modeling the diurnal tifde with dissipation derived from UARS/HRDI measurements, *Ann. Geophys.*, **15**, 1198, 1997

Hagan, M. E., Comparative effects of migrating solar sources on tidal signatures in the middle and upper atmosphere, *J. Geophys. Res.*, **101**, 21213, 1996

Hagan, M. E., J. M. Forbes, and F. Vial, On modeling migrating solar tides, *Geophys. Res. Lett.*, **22**, 893, 1995

Hays, P. B. et al. The high-resolution Doppler imager on the Upper Atmosphere Research Satellite, *J. Geophys. Res.*, **98**, 10,713, 1993

Hays, P. B., D. L. Wu, and the HRDI science team, Observations of the diurnal tide from space, *J. Atmos. Sci.*, **51**, 3077, 1994

Hines, C. O., Doppler-spread parameterization of gravity-wave momentum deposition in the middle atmosphere, 1, Basic formulation, *J. Atmos. Solar Terr. Phys.*, **59**, 371, 1997a

Hines, C. O., Doppler-spread parameterization of gravity-wave momentum deposition in the middle atmosphere, 2, Broad and quasi monochromatic spectra, and implementation, *J. Atmos. Solar Terr. Phys.*, **59**, 387, 1997b

Jacobi, C. et al., Mesopause region semidiurnal tide over Europe as seen from ground-based wind measurements, *Adv. Space Res.*, **24**, 1545, 1999

Lindzen R. S., Turbulence and stress due to gravity wave and tidal breakdown, *J. Geophys., Res.*, **86**, 9707, 1981

Lindzen, R. S., and S. Hong, Effects of mean winds and horizontal temperature gradients on solar and lunar semidiurnal tides in the atmosphere, *J. Atm. Sci.*, **31**, 1421, 1974

Manson, A. H., C. E. Meek, H. Teitelbaum, F. Vial., R. Schminder, D. Kuerschner, M. J. Smith, G. J. Fraser, and R. R. Clark, Climatology of semi-diurnal and diurnal tides in the middle atmosphere (70-110 km) at middle latitudes (40-55^{o}), *J. Atm. Terr. Phys.*, **51**, 579, 1989

Mayr, H. G., J. G. Mengel, C. A. Reddy, K. L. Chan, and H. S. Porter, The role of gravity waves in maintaining the QBO and SAO at equatorial latitudes, *Adv. Space Res.*, 24, 1541, 1999

Mayr, H. G., J. G. Mengel, K. L. Chan, and H. S. Porter, Seasonal variations of the diurnal tide induced by gravity wave filtering, *Geophys. Res. Lett.*, **25**, 943, 1998

McLandress, C., G. G. Shepherd, and B. H. Solheim, Satellite observations of thermospheric tides: Results from the Wind Imaging Interferometer on UARS, *J. Geophys. Res.*, **101**, 4093, 1996

McLandress, C., Sensitivity studies using the Hines and Fritts gravity wave drag parameterization, *NATO ASI Series*, Vol. I 50, 245, 1997

Miyahara, S., and J. M. Forbes, Interactions between gravity waves and the diurnal tide in the mesosphere and lower thermosphere, *J. Meteor. Soc. Japan*, **69**, 523, 1991

Strobel, D. F., Parameterization of atmospheric heating rate from 15 to 120 km due to O2 and O3 absorption of solar radiation, *J. Geophys. Res.*, **83**, 7963, 1978

Norton, W. A., and J. Thuburn, The two-day wave in a middle atmosphere GCM, *Geophys. Res. Lett.*, **23**, 2113, 1996

Norton, W. A., and J. Thuburn, Sensitivity of mesospheric mean flow, planetary waves and tides to strength of gravity wave drag, J. *Geophys. Res.*, **104**, 30,897, 1999

Vial, F., and J. M. Forbes, Recent progress in tidal modeling, *J. Atm. Terr. Phys.*, **51**, 663, 1989

Vincent, R. A., T. Tsuda, and S. Kato, Asymmetries in mesospheric tidal structure, *J. Atm. Terr. Phys.*, **51**, 609, 1989

Volland, H., *Atmospheric Tidal and Planetary Waves*, Kluwer Academic Publ., Boston, MA, 1988

Yudin, V. A., B. V. Khattatov, M. A. Geller, et al., Thermal tides and studies to tune the mechanistic tidal model using UARS observations, *Ann. Geophys.*, **15**, 1205, 1997

Zhu, X, Radiative cooling calculated by random band models with S-1-beta tailed distribution, *J. Atmos. Sci.*, **46**, 511, 1989

Figures Captions

Figure 1. Block diagram illustrating the organization of the model and interactions between different dynamical components. The planetary waves generated in the model are discussed in the companion paper (Mayr *et al.*, 2000b).

Figure 2. Adopted height variation of the eddy viscosity, which is related to the GW interaction employed in the model.

Figure 3. Snapshot of the computed zonal mean (m = 0) temperature and zonal wind fields for December solstice.

Figure 4. Contour plot of seasonal variations in the computed meridional wind amplitude for the diurnal tide at 95-km altitude. At latitudes near 20° north the maxima around equinox are observed.

Figure 5. Seasonal variations of amplitude and phase of meridional winds for the diurnal tide at 95 km and 18° north, a Gaussian point. Note the large maxima during the spring and fall seasons. The large variations on time scales of several days are produced by planetary waves generated internally (i.e., without external forcing).

Figure 6. Contour plot with logarithmic intervals of computed meridional wind amplitudes of the diurnal tide at 18° north. Note the complicated patterns of seasonal variations in different altitude regimes.

Figure 7. Amplitude and phase for meridional winds at 95 km, computed with standard GW momentum source (solid line and large + marks) and without source (dotted line and small + marks). Note the large differences between the solutions, thus revealing the importance of the GW interaction for the seasonal variations of the tide. The GW source also shifts the phase to earlier local times moving it closer to the observed values. (The computed phase of the diurnal tide occurred too early in our earlier model (Mayr et al., 1999) that employed a larger GW flux.)

Figure 8. Planetary waves for m = 3 at 95 km and 18° north computed with and without GW momentum source. These waves are believed to be initiated by the baroclinic instability, which is caused by the temperature reversal in the mesosphere that in turn is driven by GW. As shown here, GW also cause the planetary waves to be amplified significantly.

Figure 9. Numerical experiment similar to that shown in Figure 7, except that the planetary waves (PW) m = 3, 4 are turned off. This shows that the presence of the PW causes the amplitude of the tide to be reduced in summer, which contributes significantly to the seasonal variations. But, as shown with Figure 8, the PW themselves are generated primary by GW.

Figure 10. Computed variations in the eddy viscosity, K, at 18° north, shown as ratio relative to the values in Figure 2. Note that at altitudes above 80 km, K tends to be larger during the spring and fall seasons when the diurnal tide is observed to peak. Numerical results from a simplified model that incorporates such variations as if they occurred globally, show that the effect is relatively small.

Figure 11. Contour plot of seasonal variations in the computed zonal wind amplitude for the semi-diurnal tide at 95-km altitude. Note the large maxima in winter at latitudes near 45° north.

Figure 12. Seasonal variations of amplitude and phase of zonal winds of the semi-diurnal tide at 90 and 95 km and 48° north, a Gaussian point. Note the large maxima in winter and the large variations on time scales of several days that are associated with planetary waves.

Figure 13. Contour plot with logarithmic intervals of computed zonal wind amplitudes for the semi-diurnal tide at 48° north. Note the complicated patterns of seasonal variations in different altitude regimes.

Figure 14. Numerical experiment similar to that shown in Figure 7, except that it applies to the semi-diurnal tide. Here, the seasonal variation in the excitation source is turned off for comparison.

Figure 15. Numerical experiment similar to that shown in Figure 14, except that the GW momentum source is turned off.

Figure 16. Numerical experiment similar to that shown in Figure 14, except that the diurnal tide is not being excited thermally.

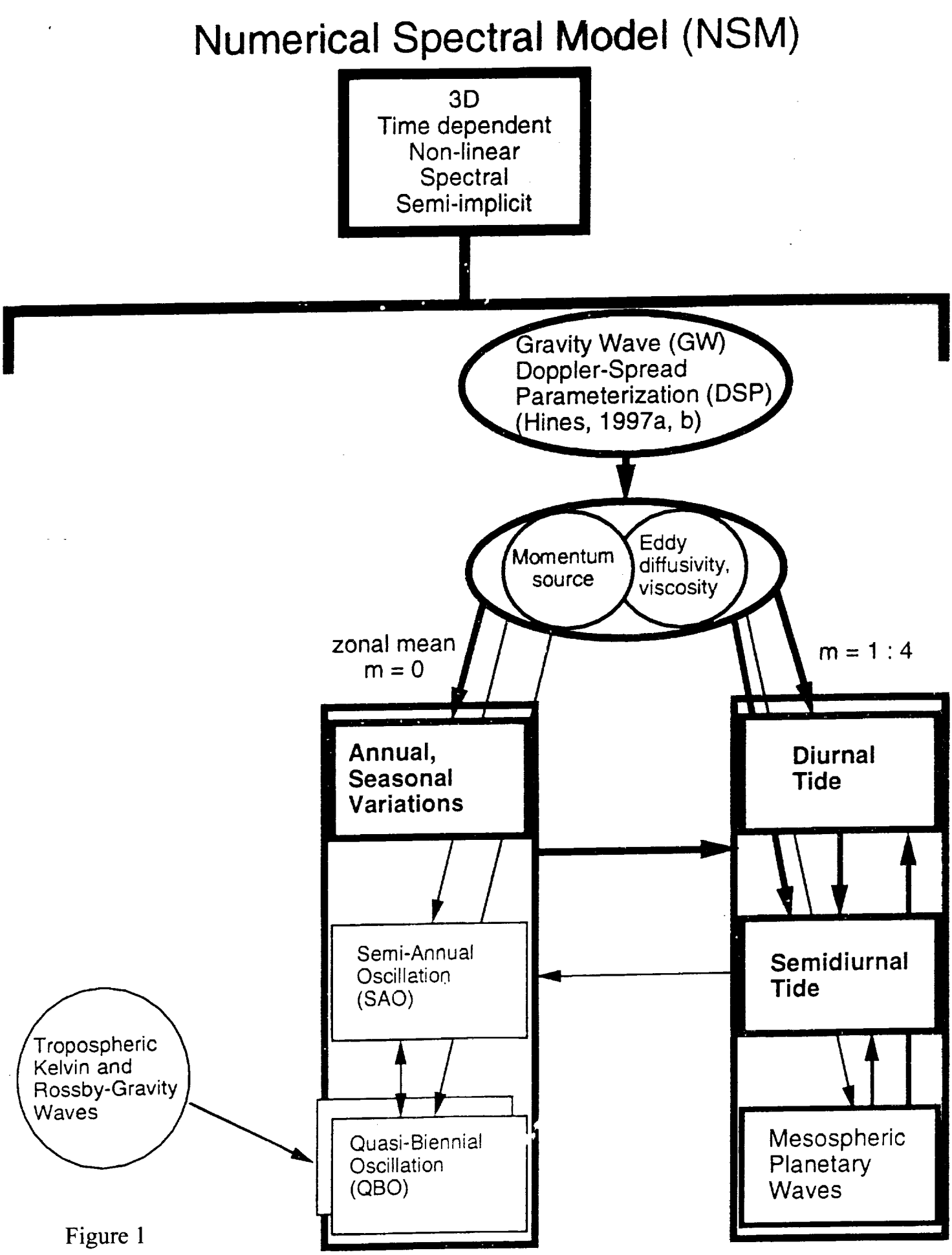
Numerical Spectral Model (NSM)
3D
Time dependent
Non-linear
Spectral
Semi-implicit
Gravity Wave (GW)
Doppler-Spread
Parameterization (DSP)
(Hines, 1997a, b)
Momentum source
Eddy diffusivity, viscosity
zonal mean
m = 0
m = 1 : 4
Annual, Seasonal Variations
Diurnal Tide
Semi-Annual Oscillation (SAO)
Semidiurnal Tide
Tropospheric Kelvin and Rossby-Gravity Waves
Quasi-Biennial Oscillation (QBO)
Mesospheric Planetary Waves

Figure 1

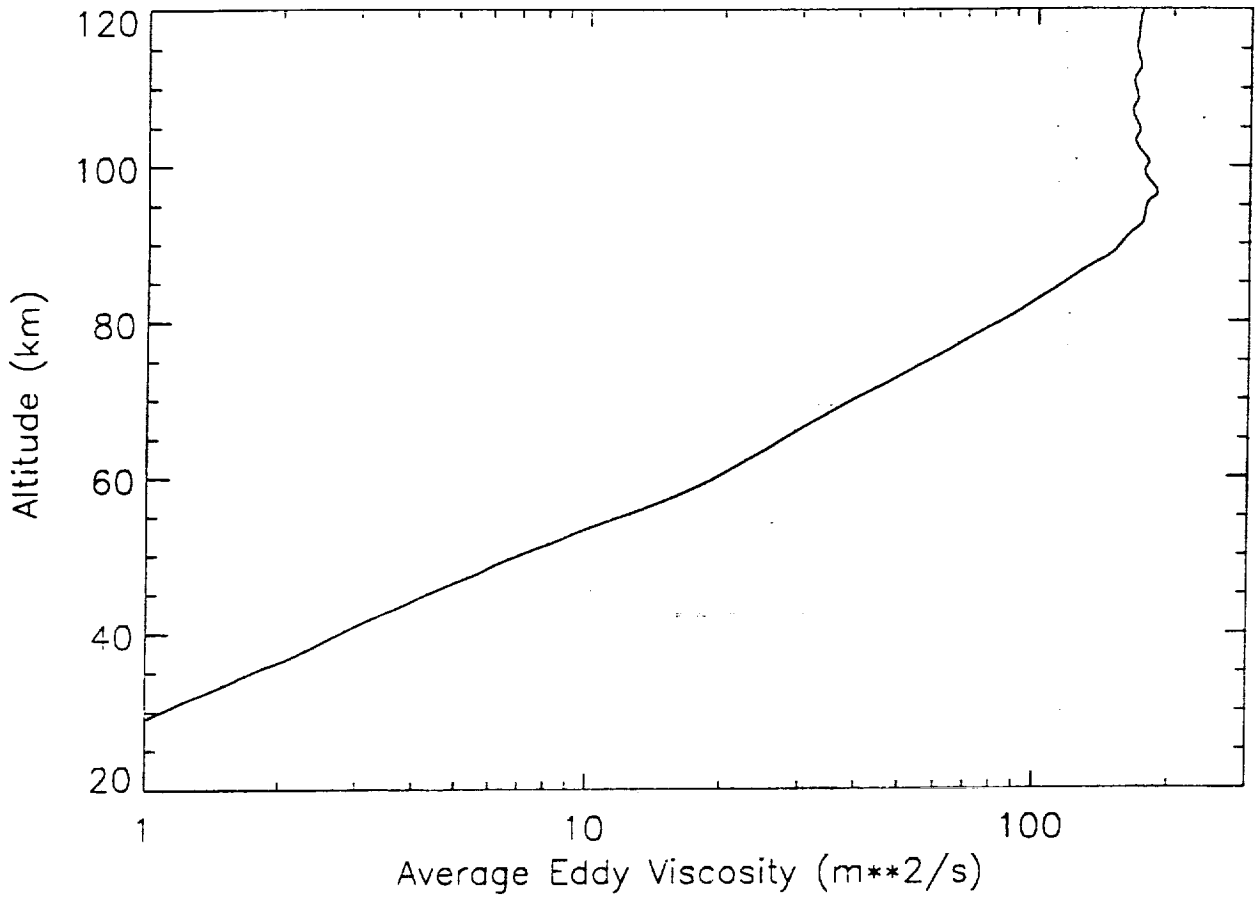
120
100
80
60
40
20
Altitude (km)
1
10
100
Average Eddy Viscosity (m**2/s)

Figure 2

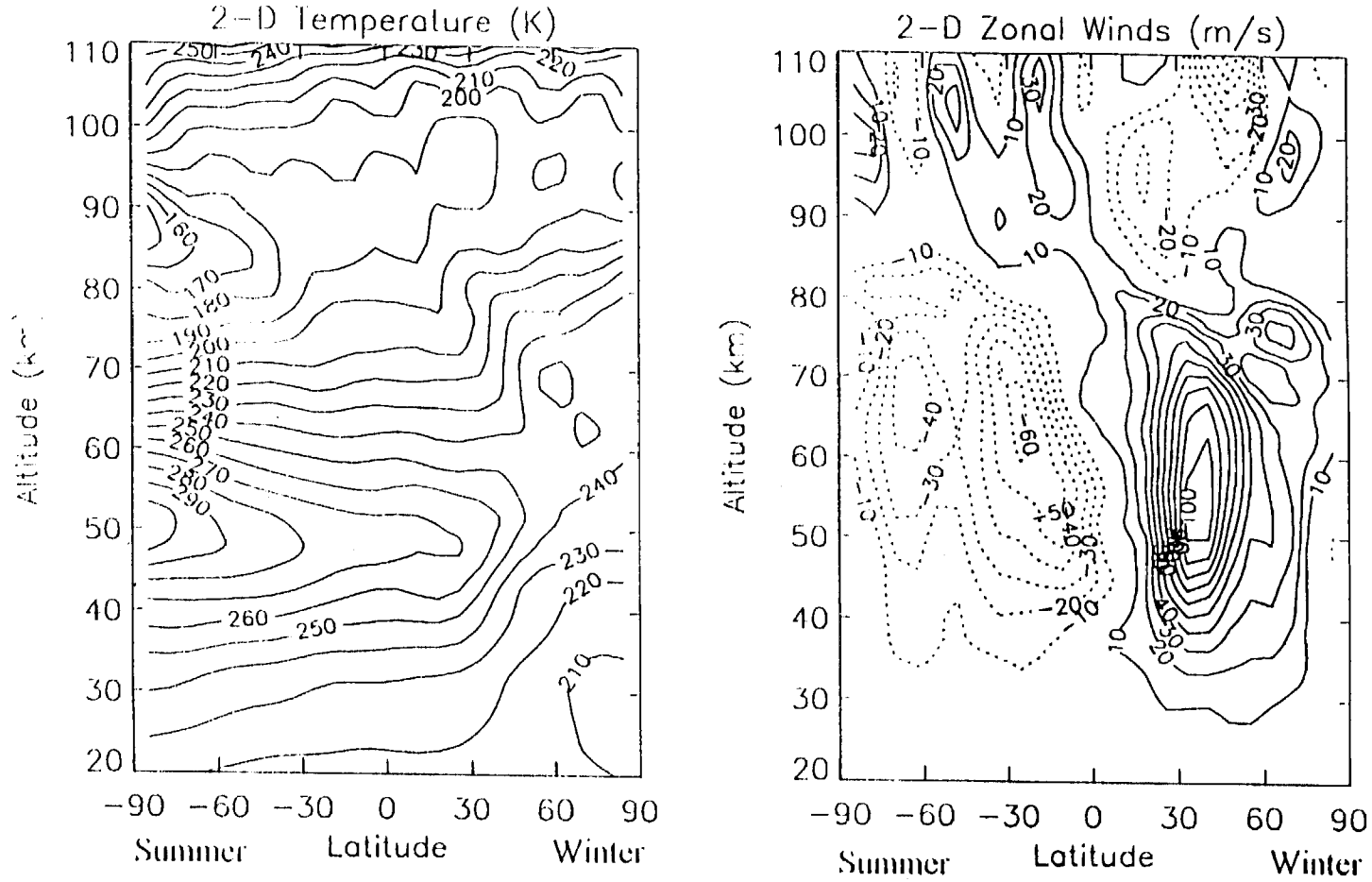
2-D Temperature (K)
Altitude (km)
110
100
90
80
70
60
50
40
30
20
-90 -60 -30 0 30 60 90
Summer
Latitude
Winter
2-D Zonal Winds (m/s)
Altitude (km)
110
100
90
80
70
60
50
40
30
20
-90 -60 -30 0 30 60 90
Summer
Latitude
Winter

Figure 3

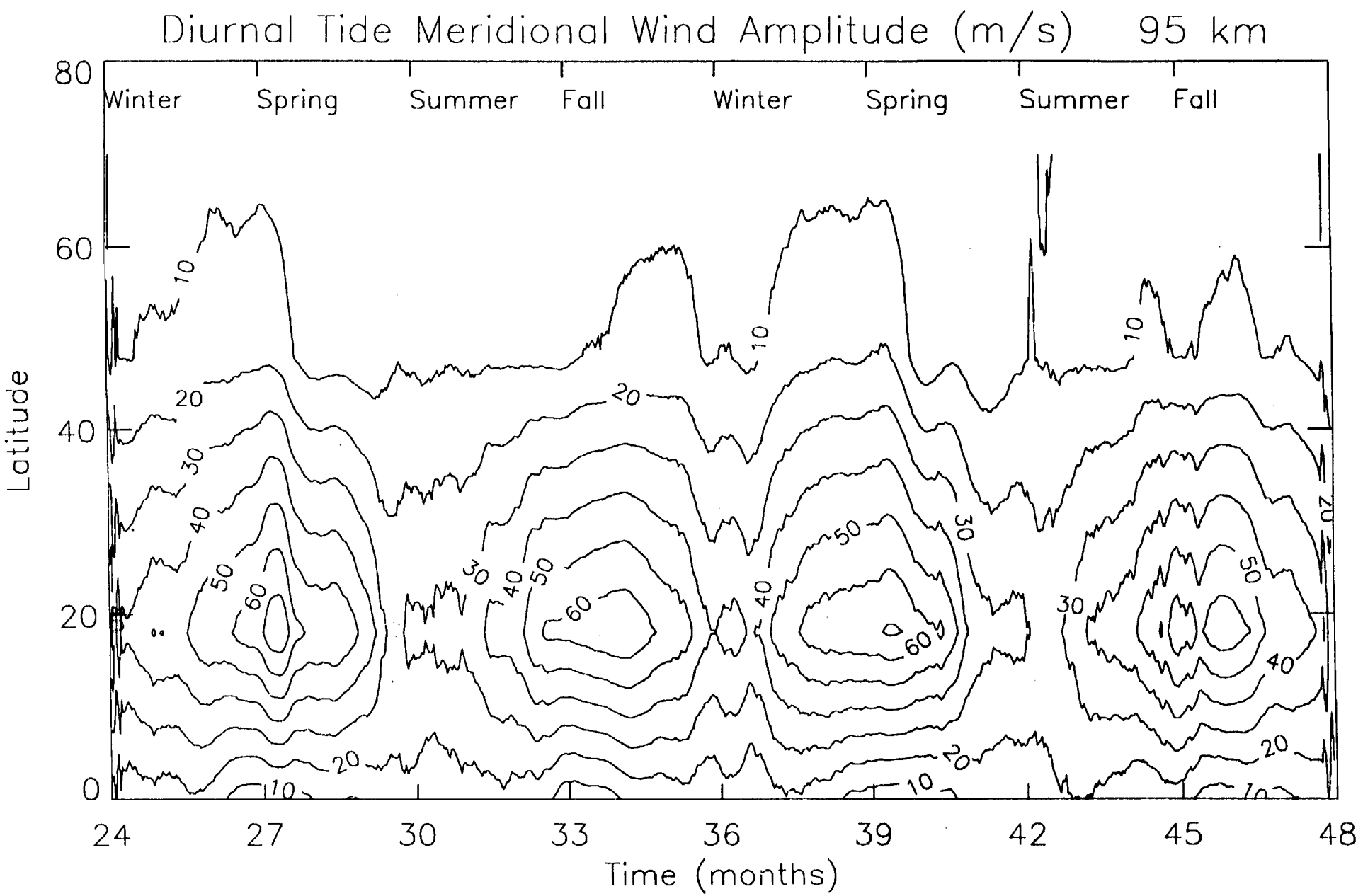
Diurnal Tide Meridional Wind Amplitude (m/s) 95 km
Winter
Spring
Summer
Fall
Winter
Spring
Summer
Fall
Latitude
80
60
40
20
0
24
27
30
33
36
39
42
45
48
Time (months)

Figure 4

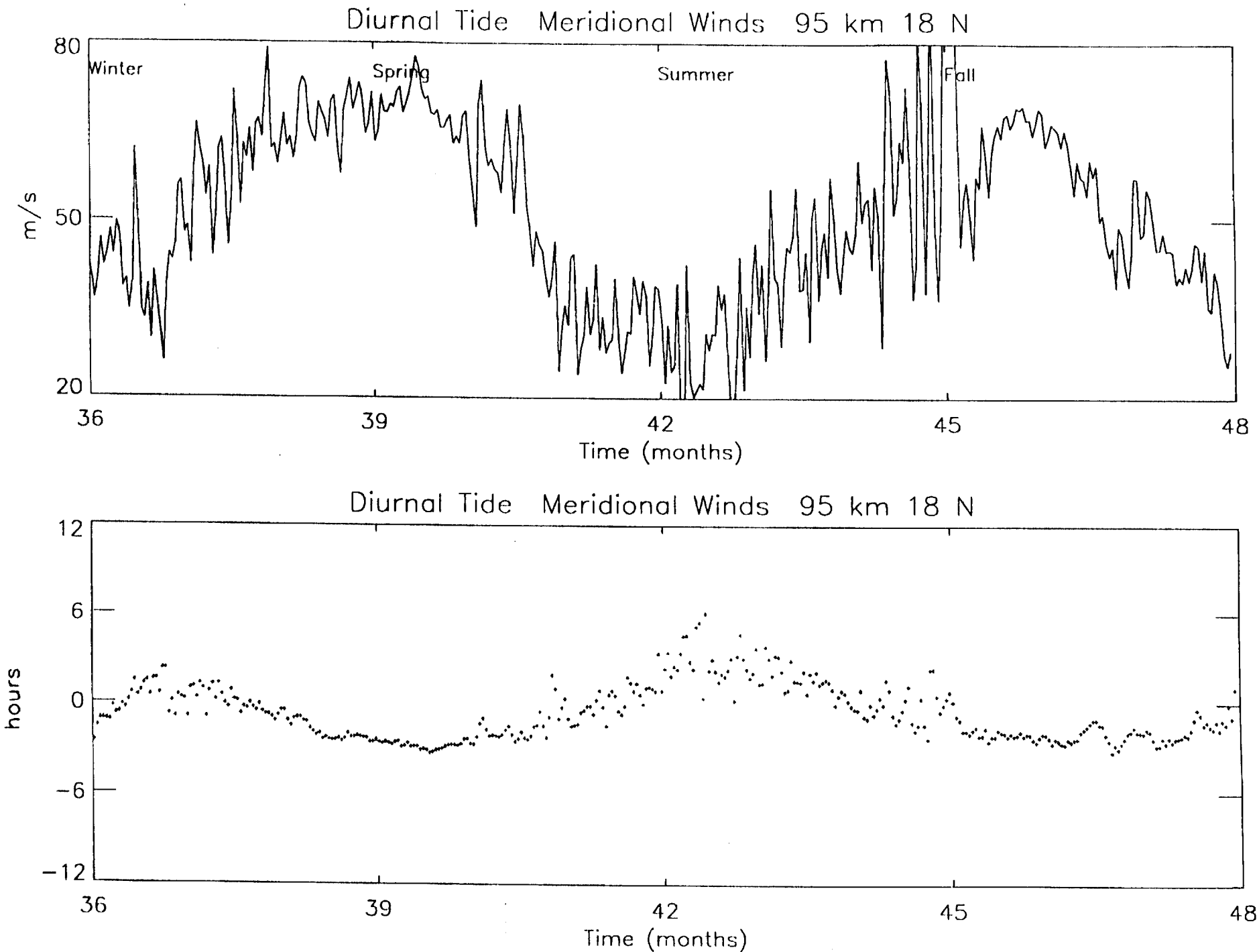
Diurnal Tide Meridional Winds 95 km 18 N
Winter
Spring
Summer
Fall
80
50
20
m/s
36
39
42
45
48
Time (months)
Diurnal Tide Meridional Winds 95 km 18 N
12
6
0
−6
−12
hours
36
39
42
45
48
Time (months)

Figure 5

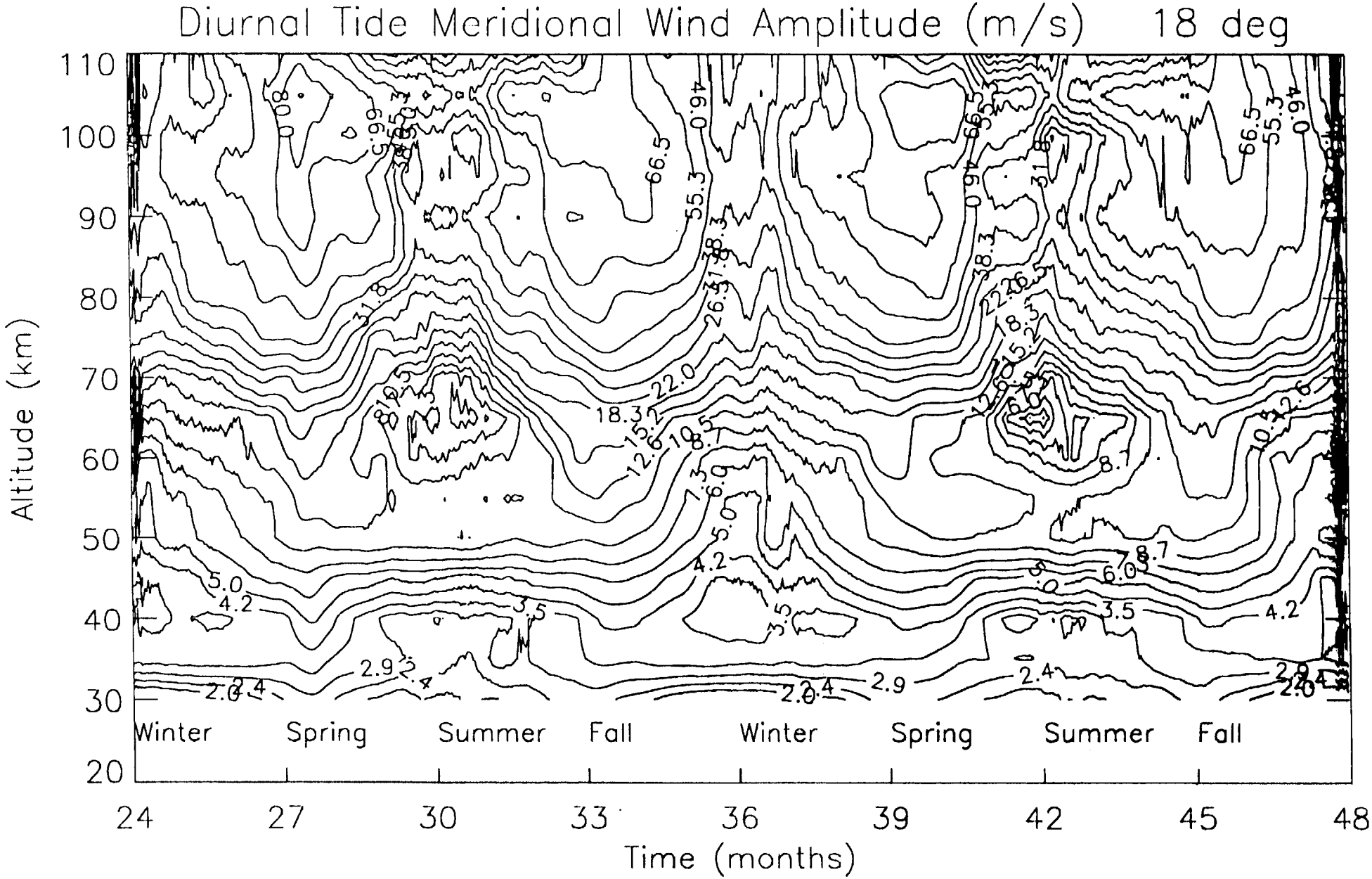
Diurnal Tide Meridional Wind Amplitude (m/s) 18 deg
Altitude (km)
110
100
90
80
70
60
50
40
30
20
Winter
Spring
Summer
Fall
Winter
Spring
Summer
Fall
24
27
30
33
36
39
42
45
48
Time (months)

Figure 6

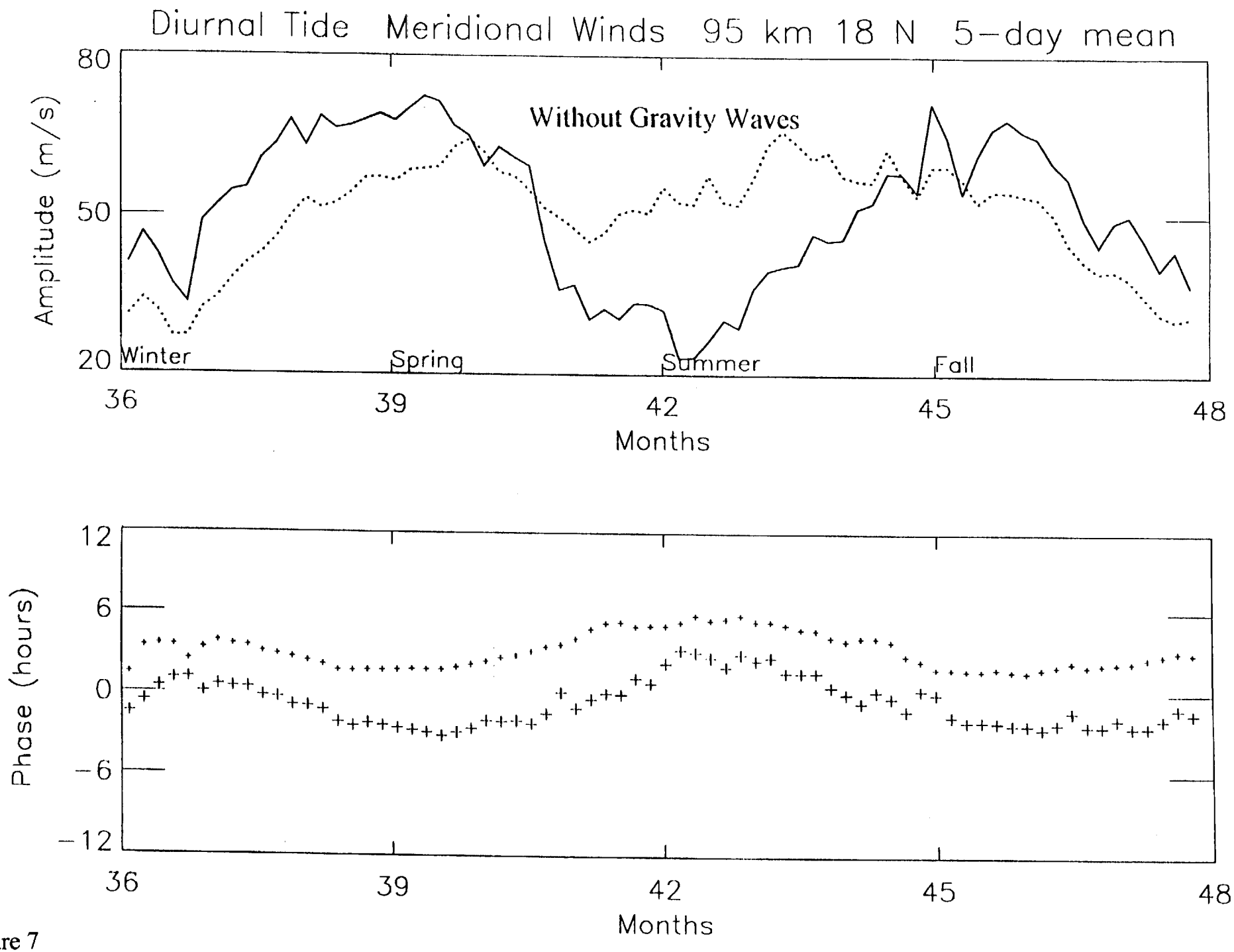
Diurnal Tide Meridional Winds 95 km 18 N 5-day mean
Without Gravity Waves
Amplitude (m/s)
80
50
20
Winter
Spring
Summer
Fall
36
39
42
45
48
Months
Phase (hours)
12
6
0
-6
-12
36
39
42
45
48
Months

Figure 7

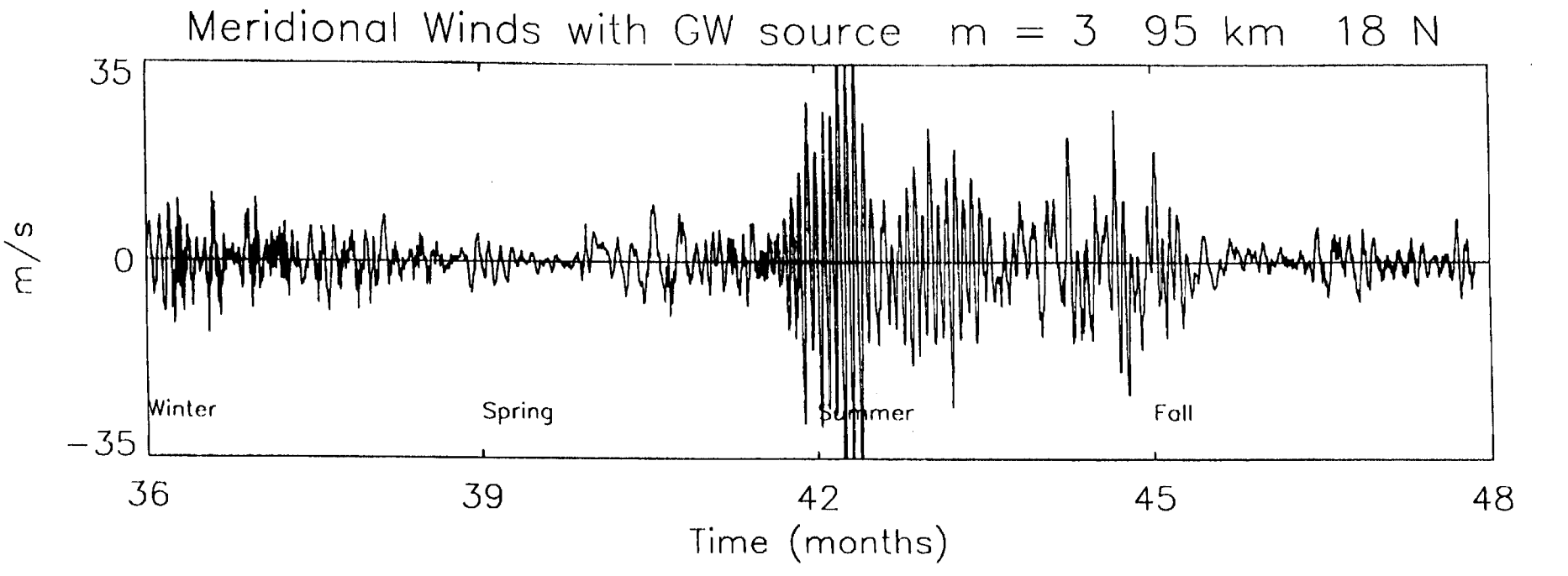
Meridional Winds with GW source m = 3 95 km 18 N
35
0
−35
m/s
Winter
Spring
Summer
Fall
36
39
42
45
48
Time (months)
D3m0

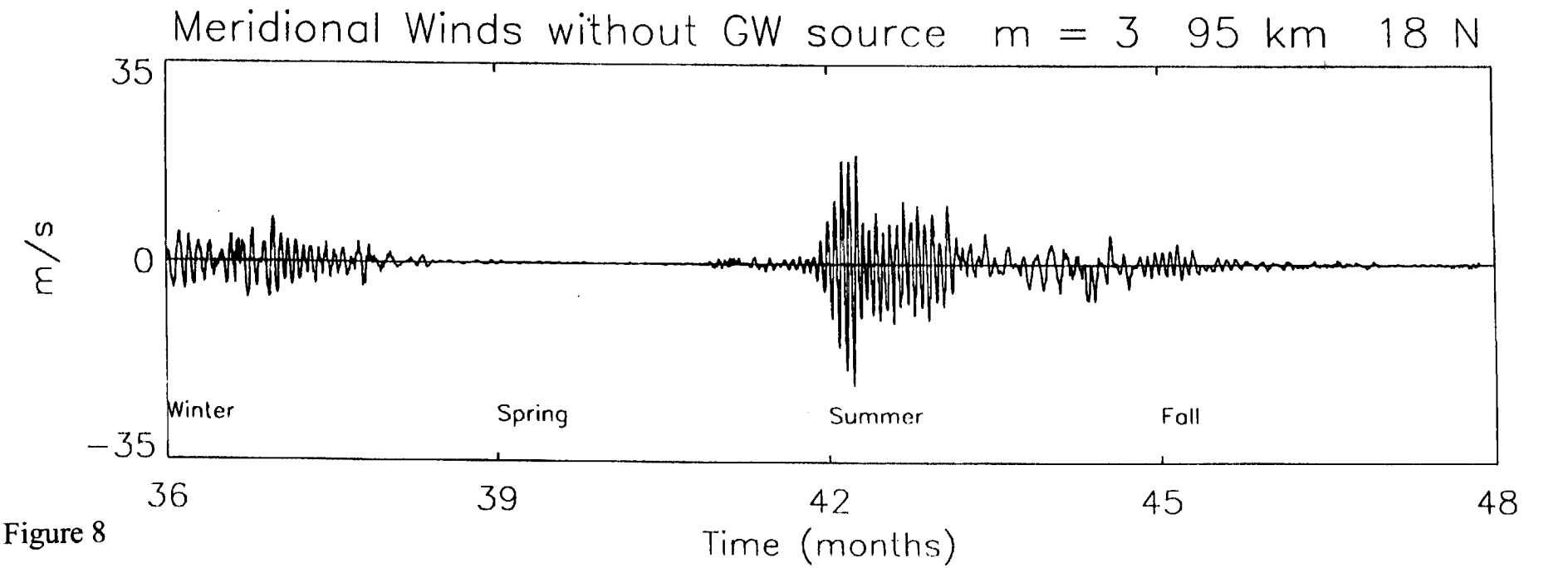
Meridional Winds without GW source m = 3 95 km 18 N
35
0
−35
m/s
Winter
Spring
Summer
Fall
36
39
42
45
48
Time (months)

Figure 8

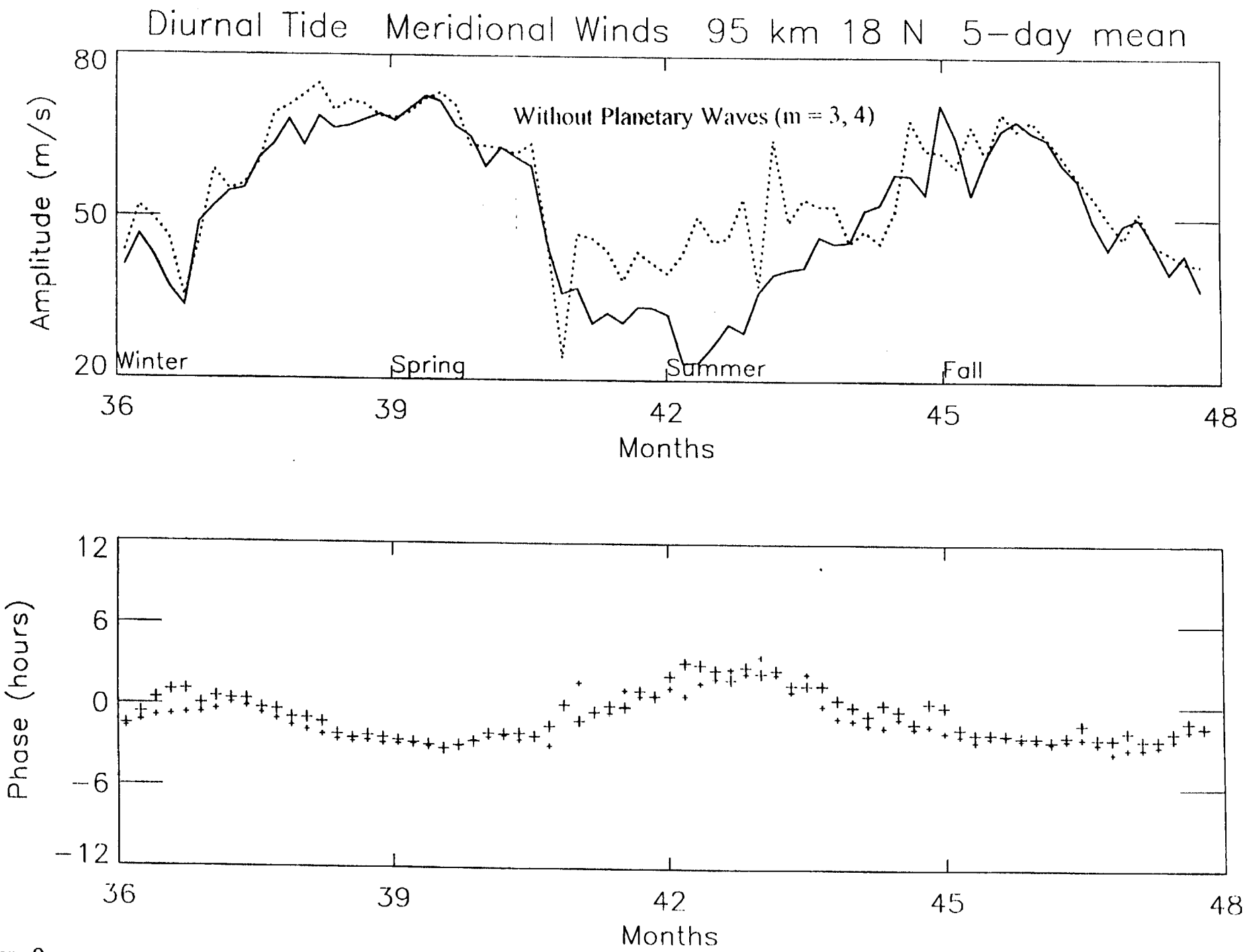
Diurnal Tide Meridional Winds 95 km 18 N 5-day mean
Without Planetary Waves (m = 3, 4)
Amplitude (m/s)
80
50
20
Winter
Spring
Summer
Fall
36
39
42
45
48
Months
Phase (hours)
12
6
0
-6
-12
36
39
42
45
48
Months

Figure 9

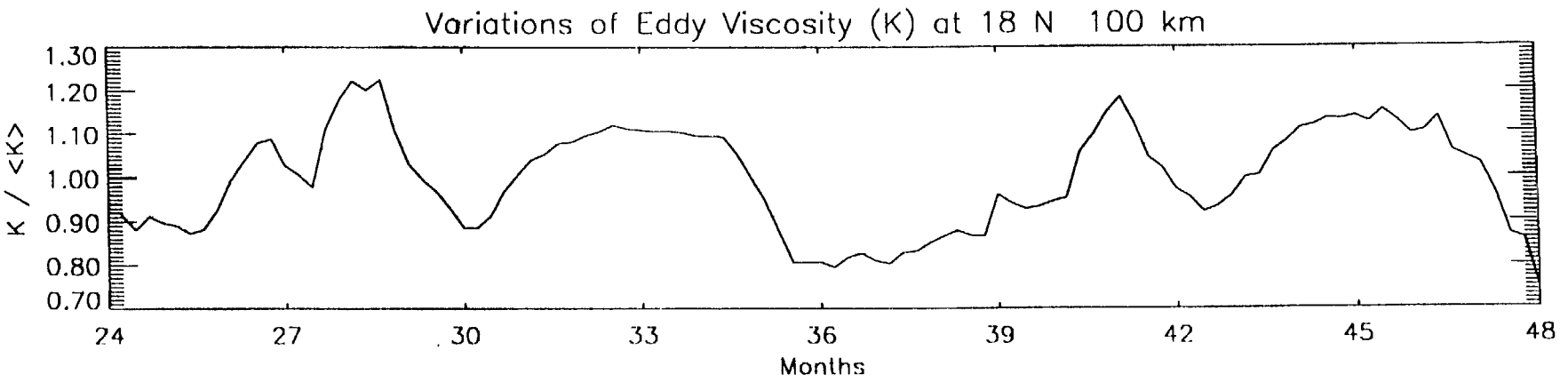

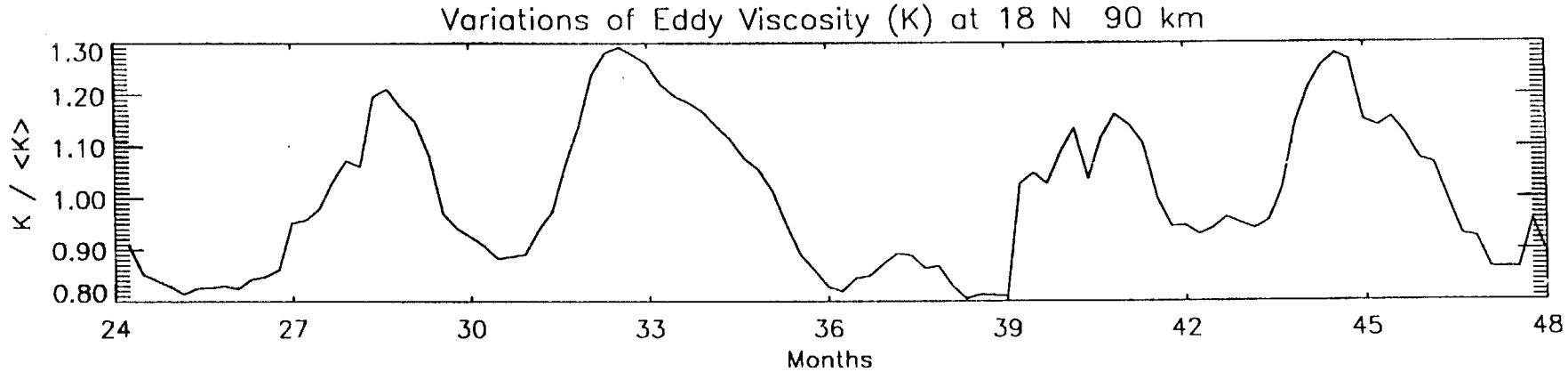

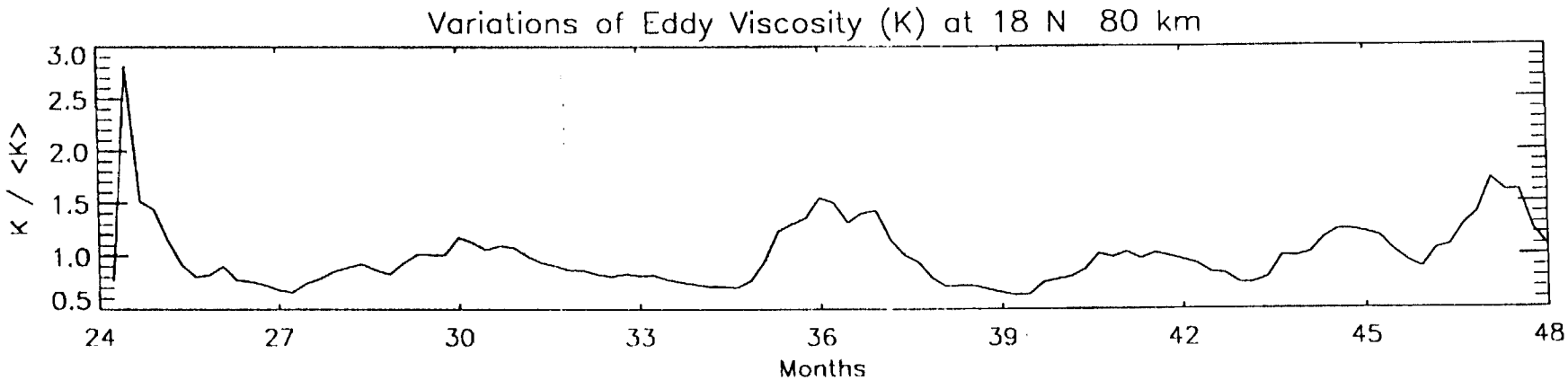

Figure 10

Winter Spring Summer Fall Winter Spring Summer Fall Winter

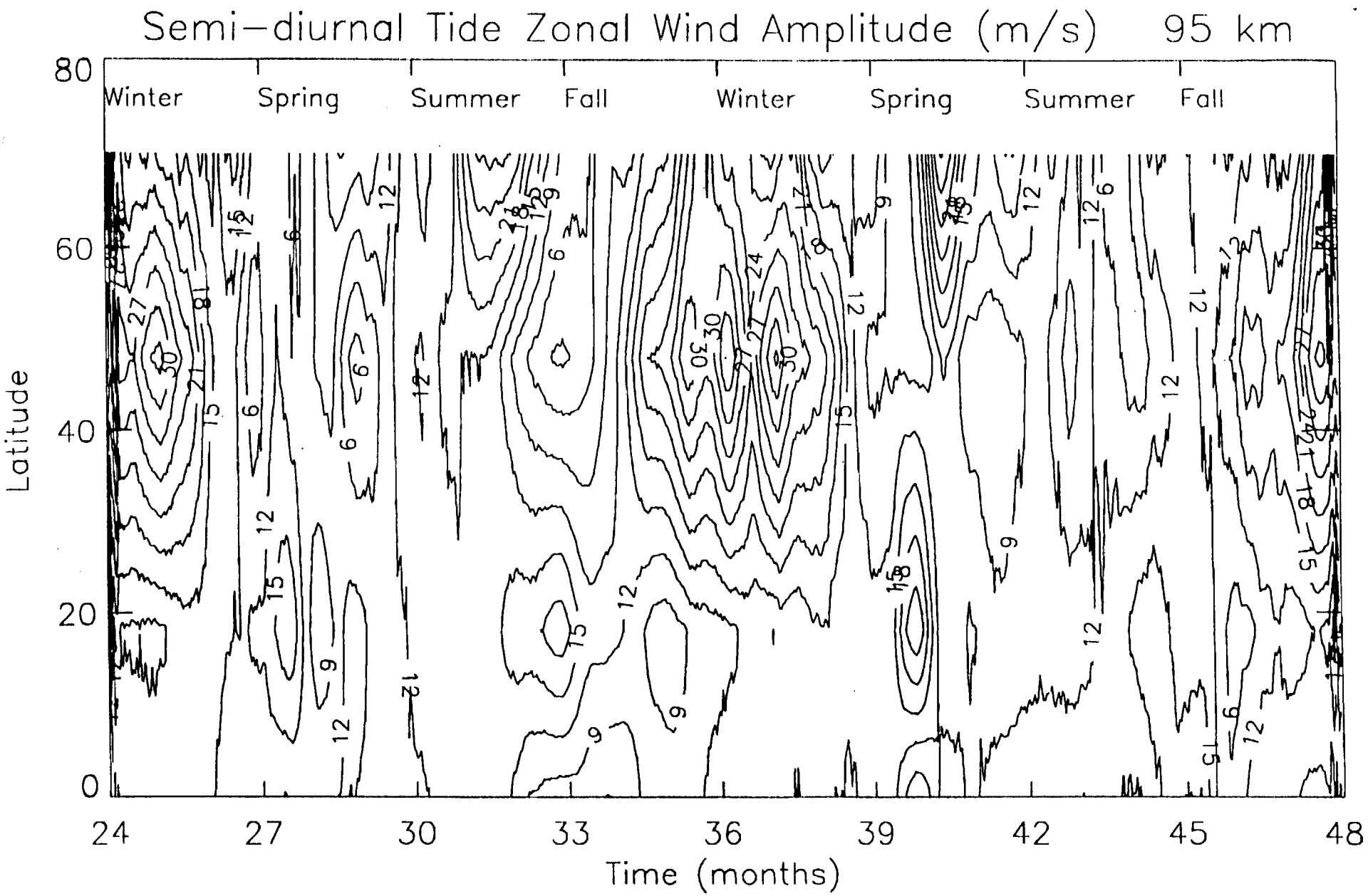
Semi–diurnal Tide Zonal Wind Amplitude (m/s) 95 km
Winter
Spring
Summer
Fall
Winter
Spring
Summer
Fall
Latitude
80
60
40
20
0
24
27
30
33
36
39
42
45
48
Time (months)

Figure 11

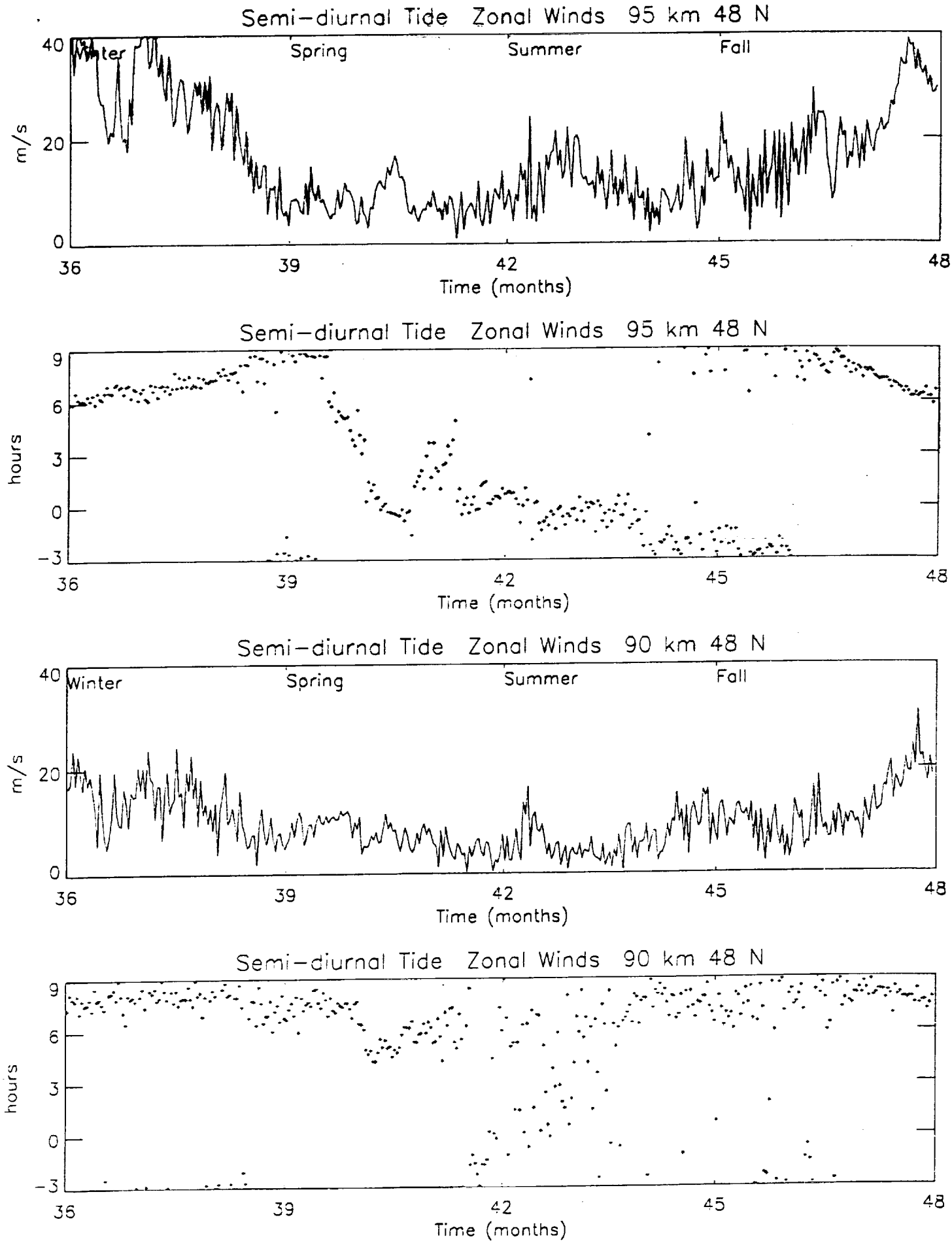
Semi−diurnal Tide Zonal Winds 95 km 48 N
Winter
Spring
Summer
Fall
m/s
40
20
0
36
39
42
45
48
Time (months)
Semi−diurnal Tide Zonal Winds 95 km 48 N
hours
9
6
3
0
−3
36
39
42
45
48
Time (months)
Semi−diurnal Tide Zonal Winds 90 km 48 N
Winter
Spring
Summer
Fall
m/s
40
20
0
36
39
42
45
48
Time (months)
Semi−diurnal Tide Zonal Winds 90 km 48 N
hours
9
6
3
0
−3
36
39
42
45
48
Time (months)

Figure 12

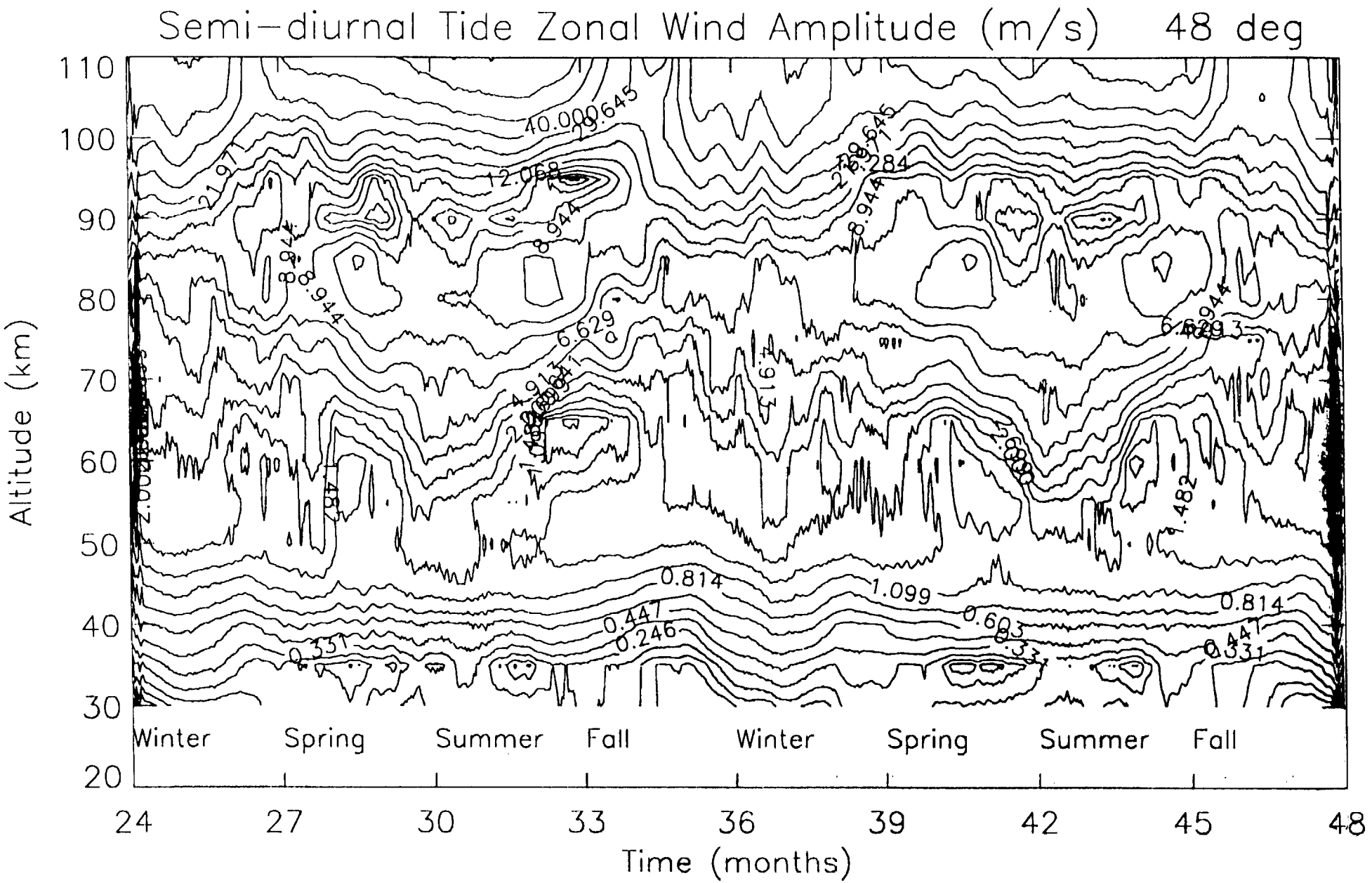
Semi−diurnal Tide Zonal Wind Amplitude (m/s) 48 deg
Altitude (km)
110
100
90
80
70
60
50
40
30
20
40.000
29.645
12.068
8.944
6.629
4.917
2.284
0.814
1.099
0.603
0.447
0.246
0.331
Winter
Spring
Summer
Fall
Winter
Spring
Summer
Fall
24
27
30
33
36
39
42
45
48
Time (months)

Figure 13

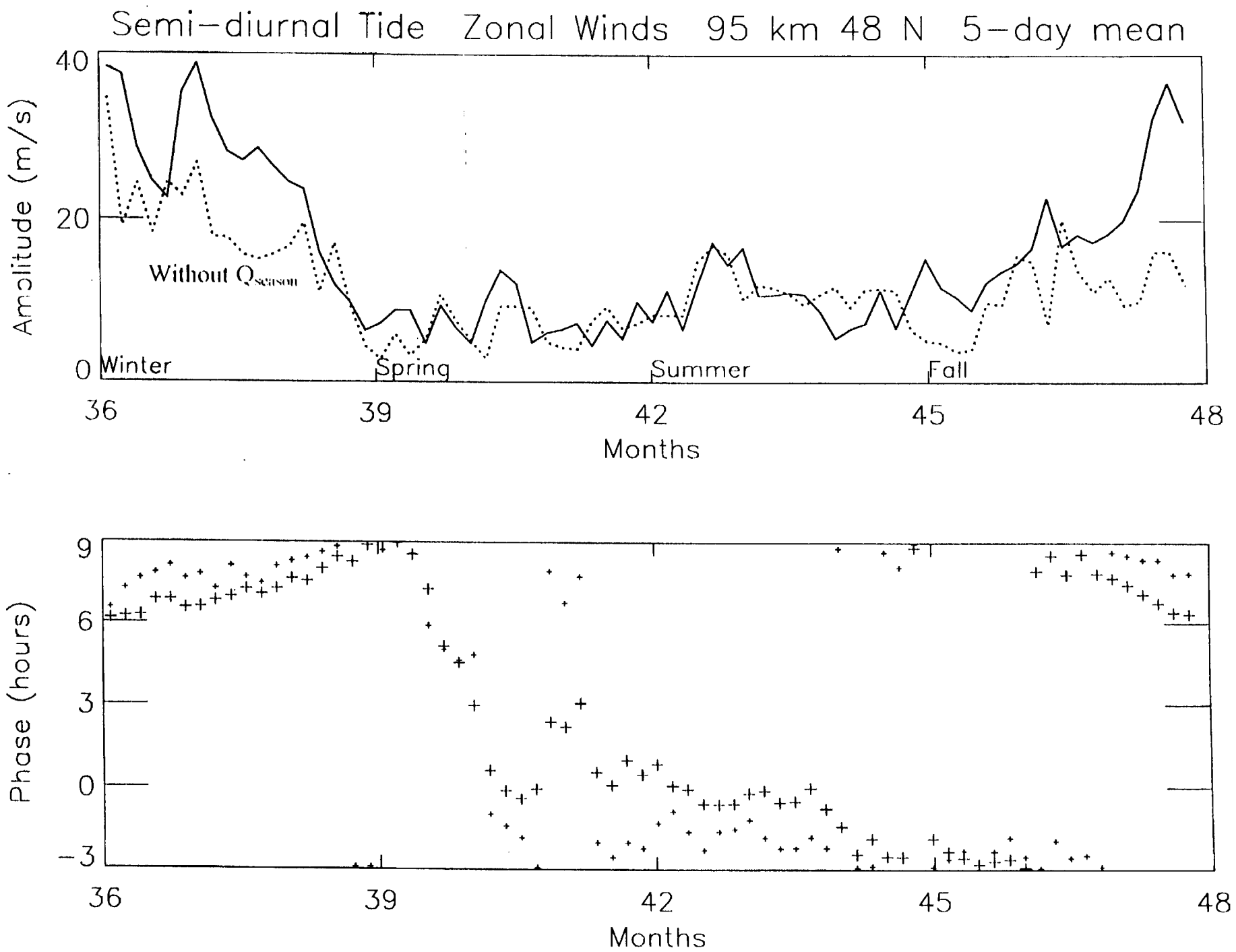
Semi-diurnal Tide Zonal Winds 95 km 48 N 5-day mean
Amplitude (m/s)
40
20
0
Without Q_{season}
Winter
Spring
Summer
Fall
36
39
42
45
48
Months
Phase (hours)
9
6
3
0
−3
36
39
42
45
48
Months

Figure 14

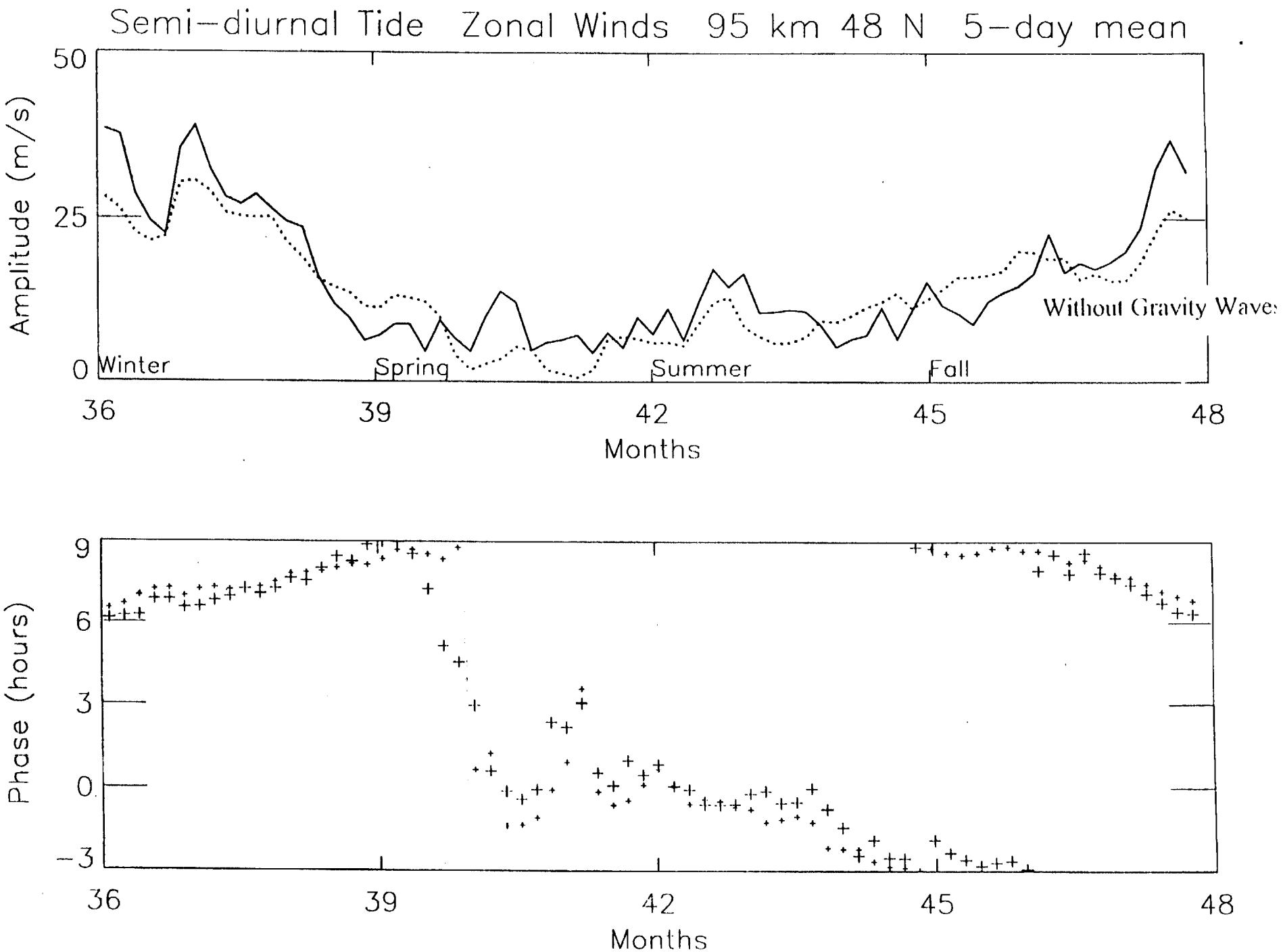
Semi–diurnal Tide Zonal Winds 95 km 48 N 5–day mean
Amplitude (m/s)
50
25
0
Winter
Spring
Summer
Fall
Without Gravity Waves
36
39
42
45
48
Months
Phase (hours)
9
6
3
0
−3
36
39
42
45
48
Months

Figure 15

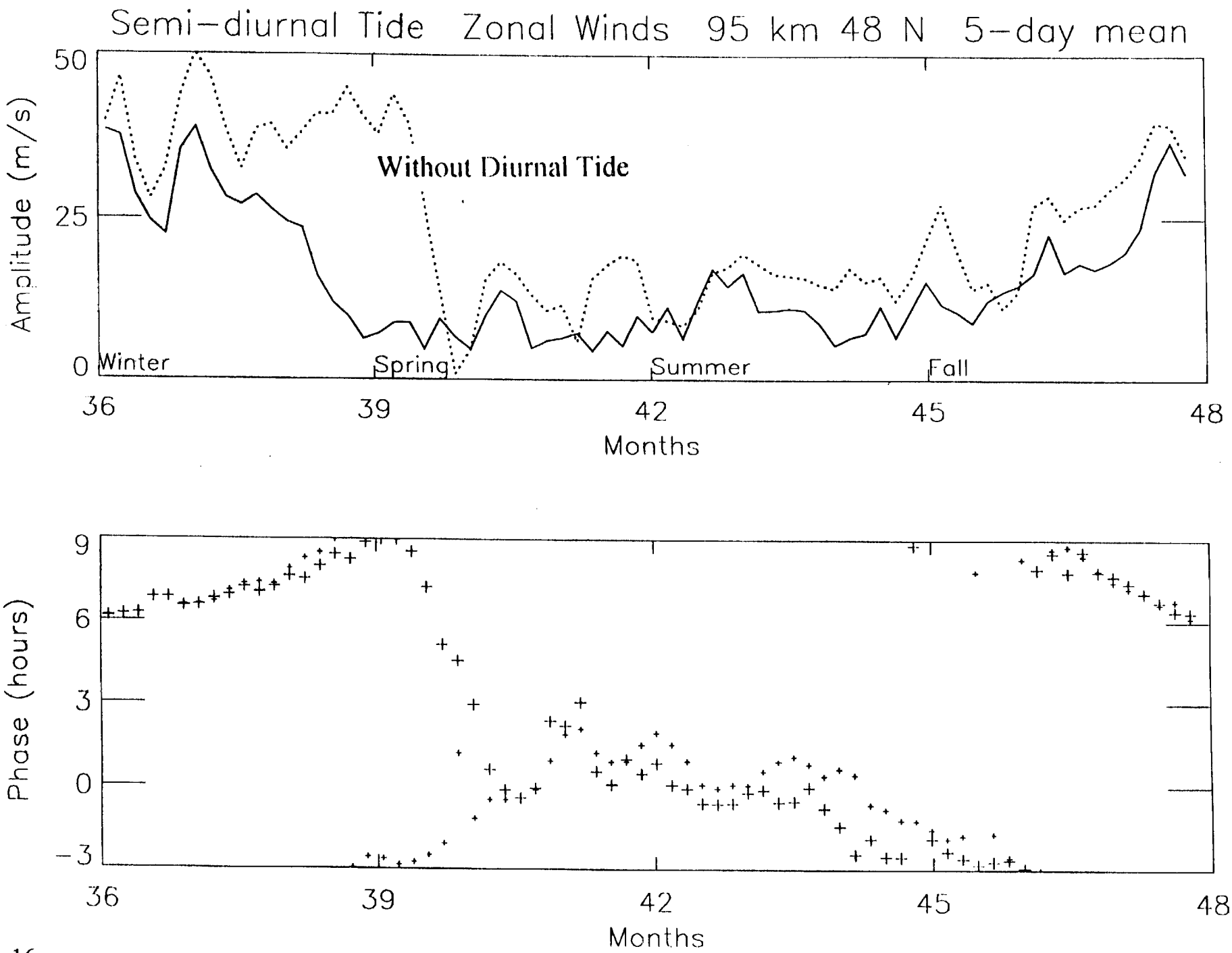
Semi-diurnal Tide Zonal Winds 95 km 48 N 5-day mean
Amplitude (m/s)
50
25
0
Without Diurnal Tide
Winter
Spring
Summer
Fall
36
39
42
45
48
Months
Phase (hours)
9
6
3
0
-3
36
39
42
45
48
Months

Figure 16

Mesosphere dynamics with gravity wave forcing: 2, Planetary waves

H. G. Mayr[1], J. G. Mengel[2], K. L. Chan[3], and H. S. Porter[4]

[1]NASA Goddard Space Flight Center, Greenbelt, MD

[2]SM&A Corporation, Vienna, VA

[3]Hong Kong University of Science and Technology, Hong Kong, China,

[4]Furman University, Greenville, SC

POPULAR SUMMARY: Large planetary waves are observed in the upper mesosphere. Yet it is not clear where they originate. Waves generated in the troposphere cannot readily propagate to these altitudes. We present results from our 3D numerical spectral model that incorporates a realistic gravity wave (GW) parameterization. In this model, planetary waves (PW) with zonal wavenumbers 1 to 4 are generated above 50 km without external time dependent forcing. The waves tend to be produced primarily during solstice conditions, which indicates that the baroclinic instability (associated with the GW driven reversal in the latitudinal temperature gradient) is playing an important role. Numerical experiments show that GW's are also directly involved in generating the PW's. The predominant wave periods vary from about 7 to 2 days for wavenumbers m = 1 to 4, respectively. A common feature of the PW's generated in summer and winter is that their vertical wavelengths throughout the mesosphere are large, which indicates that the waves are not propagating freely but are generated throughout the region. Another common feature is that the PW's propagate preferentially westward in summer and eastward in winter, being launched from the westward and eastward zonal winds that prevail respectively in summer and winter at altitudes below 80 km.